Supplementary to: Revised direct radiative forcing of airborne microplastics suggests warming

Felix W. Goddard[1,*], Stefania Glukhova[2], Eric C. Le Ru[2], Nikolaos Evangeliou[3], Cameron McErlich[1], Catherine Hardacre[1], Dave Frame[1], Peter Kuma[4], and Laura E. Revell[1,*]

[1]School of Physical and Chemical Sciences, University of Canterbury, Christchurch, New Zealand
[2]The MacDiarmid Institute for Advanced Materials and Nanotechnology, School of Chemical and Physical Sciences, Victoria University of Wellington, Wellington, New Zealand
[3]Stiftelsen NILU (formerly NILU - Norwegian Institute for Air Research), Department for Atmospheric & Climate Research (ATMOS), 2007 Kjeller, Norway
[4]Rossby Centre, Swedish Meteorological and Hydrological Institute, Norrköping, Sweden
*Corresponding authors: felix.goddard@pg.canterbury.ac.nz and laura.revell@canterbury.ac.nz

S1 Variation of forcing efficiency with surface albedo

Supplementary Fig. S1a–c shows the dependence of the longwave, shortwave, and net IRF efficiency on the shortwave albedo of the underlying surface. The forcing efficiency is independent of the surface MP concentration, hence panels (a) and (b), showing the uniform and non-uniform MP spatial distributions respectively, are the same. The general pattern is the same across all of our experiments (not shown), i.e. the longwave forcing efficiency is close to constant across the range of surface albedos, while the shortwave forcing efficiency increases as surface albedo increases. The shortwave forcing efficiency is very well constrained by its surface albedo dependence, whereas the longwave forcing is more uncertain, likely due to the influence of atmospheric moisture on the longwave transmittance.

Hatching in Supplementary Fig. S1b shows areas where the surface MP number concentration is < 1 MP m^{-3} (when scaled to a global-average surface MP concentration of 3.99 MP m^{-3} between 50 and 100 µm diameter). Large areas of the ocean (i.e. low albedo surfaces) have low MP concentrations; this is illustrated in Supplementary Fig. S1d, which plots the total MP burden found over surfaces with a given albedo. The lowest albedo value (~ 0.07) includes all ocean surfaces, and has a 70% smaller MP burden for the non-uniform horizontal distribution than for the uniform one.

This relationship between radiative forcing and surface albedo accords with that described for other aerosol species[1,2,3]; however, Yang et al.[4] in a modelling study of MP radiative effects find a longwave forcing that decreases with albedo and a shortwave forcing that is a concave function of albedo, increasing at low albedo, peaking around ~ 0.5, and decreasing for higher values. The reason for this difference in behaviour is not clear, but may be due to differences in the radiative transfer model used.

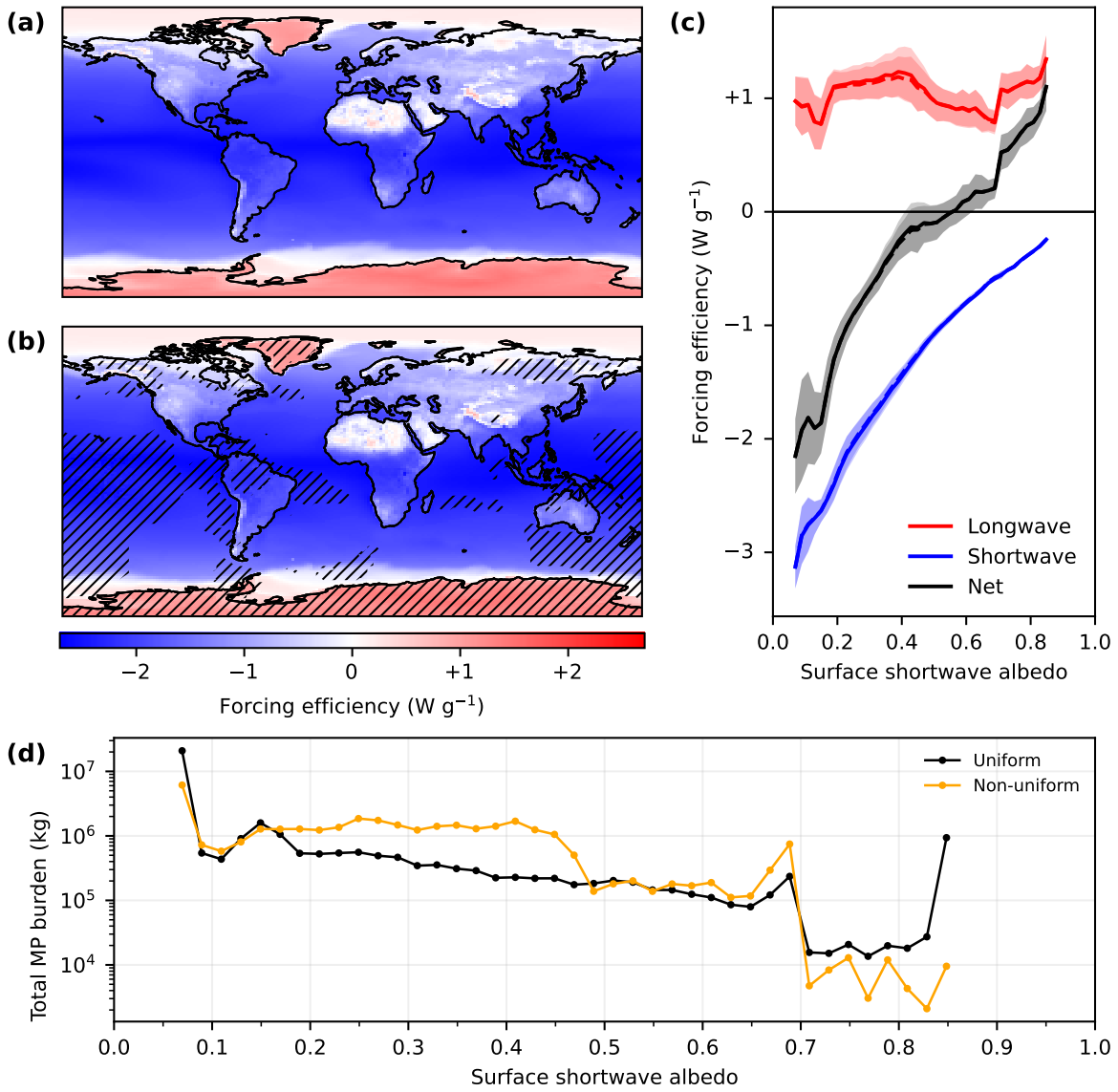

Figure S1: Spatial distribution of net IRF efficiency for experiments (a) 'Reference' and (b) 'Spatially non-homogeneous'; forcing efficiency here is calculated per-grid cell as the net forcing [W m^{-2}] per unit column MP mass density [g m^{-2}] hence has units W g^{-1}. Hatching on panel (b) indicates regions where the scaled surface MP concentration is less than 1 MP m^{-3}. (c) Dependence of net IRF efficiency on surface shortwave albedo for the same two simulations; solid lines indicate the 'Reference' experiment while dashed lines indicate the 'Spatially non-homogeneous' experiment. Each curve was calculated by dividing surface albedo into 40 evenly-spaced bins between the minimum and maximum values (0.07 and 0.85 respectively); the mean IRF efficiency (line) and and one standard deviation (shaded region) for each bin were calculated from those grid cells with a surface albedo falling in that bin. (d) Total MP burden divided into the same bins of surface shortwave albedo for the two horizontal MP distributions. Both distributions were scaled to a global-average surface concentration of 1 MP m^{-3} (and hence also the same total plastic burden, 3.36×10^7 kg) for comparability.

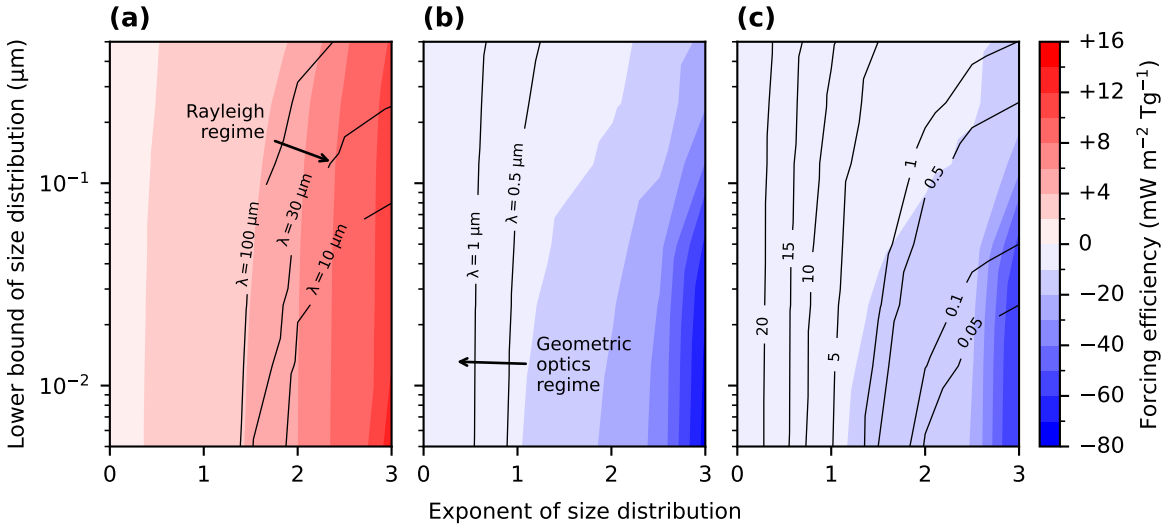

Figure S2: Variation of the net forcing efficiency of MPs following a power law size distribution as a function of the power law exponent α (see Equation 2) and the lower bound of the distribution. Panels (**a**), (**b**), and (**c**) show the longwave, shortwave, and net components of the forcing efficiency respectively. Contours on (**a**) show the average particle radius r that yields $2\pi r/\lambda = 0.1$ for the indicated wavelengths λ (chosen to be representative of the longwave band); this corresponds to the Rayleigh regime of Mie theory ($r \ll \lambda$). Contours on (**b**) show the average particle radius r that yields $2\pi r/\lambda = 100$ for the indicated wavelengths λ (chosen to be representative of the shortwave band); this corresponds to the Geometric optics regime of Mie theory ($r \gg \lambda$). Contours on (**c**) show the average particle radius in µm. Note that we set the lower bound of the size distribution to 1 µm, as discussed in the text, but show here lower bounds as small as 0.01 µm to demonstrate the importance of constraining size distribution to determine nanoplastic radiative forcing.

S2 Variation in parameters of the power law size distribution

Supplementary Fig. S2 shows the MP radiative forcing efficiency across a range of values of the exponent α and the lower radius bound in the power law size distribution (Equation 7 in the main text). Leusch et al.[5] report power law exponents in the range 1 to 2 for MPs across a range of environmental matrices.

We calculate forcing efficiency as the ratio of radiative forcing to total MP burden. As such, they are sensitive to the average particle volume: smaller particles produce a higher particle number concentration for the same mass burden, giving a higher optical depth. However, absorption and scattering cross sections scale with the particle cross-sectional area ($\sigma \propto r^2$) in the geometric optics regime ($r \gg \lambda$) and with the sixth power of radius ($\sigma \propto r^6$) in the Rayleigh regime ($r \ll \lambda$), hence become smaller for smaller particles. These two effects are in competition as the average particle size decreases.

Increasing the exponent of the power law causes the distribution to favour smaller particles and to produce stronger forcing efficiencies. Decreasing the lower bound of the size distribution similarly produces smaller particles and stronger forcing efficiencies, though for exponents < 1 this effect is very weak. It can also be seen that shortwave forcing efficiencies increase in magnitude faster than longwave forcing efficiencies, such that the net forcing efficiency is increasingly negative when moving to larger exponents or lower minimum radii. The greatest magnitude of net forcing efficiency we show in Supplementary Fig. S2c is -62.7 mW m^{-2} Tg^{-1} at an exponent $\alpha = 3$ and lower bound of 0.01 µm diameter.

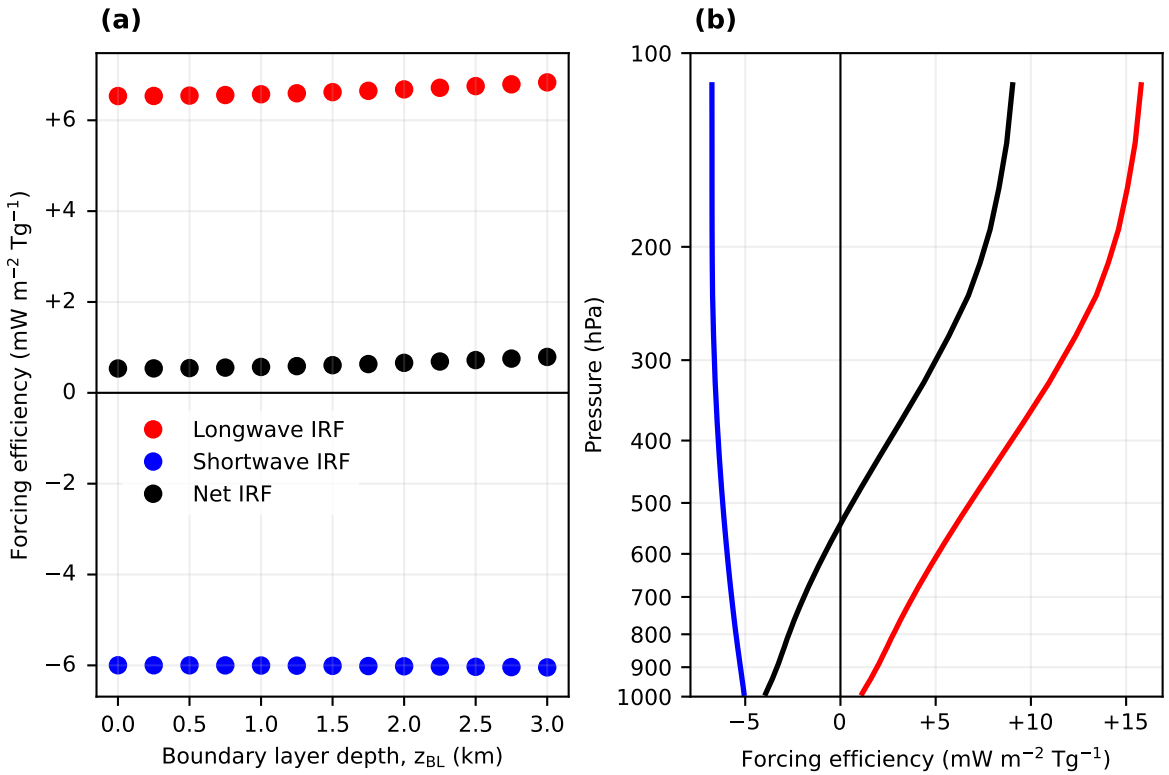

Figure S3: (a) Change in IRF efficiency with variation in the depth of the well-mixed boundary layer (z_{BL} in Equation (11)); throughout the main text, a value of $z_{\mathrm{BL}} = 2$ km is assumed. (b) Variation in IRF efficiency with altitude.

S3 Variation in forcing efficiency with microplastic altitude

Supplementary Fig. S3a shows how the forcing efficiency of the 'Whole troposphere' experiment (using the vertical distribution given by Equation 11 in the main text) varies with choice of z_{BL}. This parameter represents the depth of the well-mixed boundary layer at the surface; throughout the main text we assume a constant $z_{\mathrm{BL}} = 2$ km, however in the real atmosphere the planetary boundary layer varies substantially in depth over different land surfaces and seasonally[6,7].

It can be seen that variations in z_{BL} between 0 and 3 km produce a negligible variation in the resulting forcing efficiency. This insensitivity to z_{BL} can be explained by the vertical variation in forcing efficiency: Supplementary Fig. S3b shows the forcing efficiency for a layer of MPs at the indicated pressure. It can be seen that both the shortwave and longwave forcing efficiencies increase in magnitude with decreasing pressure (increasing altitude). The longwave forcing efficiency in particular increases rapidly enough that at pressures lower than $\sim$ 550 hPa (altitudes greater than $\sim$ 5 km) the net forcing efficiency becomes positive.

This implies that it is the extent of the MP vertical distribution rather than the choice of z_{BL} that produces the increase in longwave and net forcing efficiency observed in the 'Whole troposphere' experiment (main text, Fig. 1), and hence a constant $z_{\mathrm{BL}} = 2$ km is not a limiting assumption.

S4 Selection of MP concentrations and scaling procedure

Leusch et al.[5] demonstrated that the size distribution function of MPs across a range of environmental compartments is well-described by a power law. In particular, for outdoor airborne MPs, their results yield the distribution function

$$\frac{\mathrm{d}N}{\mathrm{d}r} = 36.6\, r^{-1.52} \tag{1}$$

where r is the particle radius in µm and N is the particle number concentration. The total number concentration within a given range of particle radius is given by the integral of this distribution function, hence between 50 and 100 µm diameter, this yields

$$N_{50-100} = \int_{25\ \mu\mathrm{m}}^{50\ \mu\mathrm{m}} 36.6\, r^{-1.52}\, \mathrm{d}r = 3.99\ \mathrm{MP\ m^{-3}} \tag{2}$$

The gamma size distribution is given by

$$\frac{\mathrm{d}N}{\mathrm{d}r} = A \left(\frac{2r}{15}\right)^2 \frac{1}{r} e^{-2r/15} \tag{3}$$

where A [MP m^{-3} µm^{-1}] is a normalisation constant. We match this distribution to the power law by choosing A such that we get the same N_{50-100}, i.e.

$$N_{50-100} = 3.99\ \mathrm{MP\ m^{-3}} = \int_{25\ \mu\mathrm{m}}^{50\ \mu\mathrm{m}} A \left(\frac{2r}{15}\right)^2 \frac{1}{r} e^{-2r/15}\, \mathrm{d}r \tag{4}$$

$$= A \times 0.145\ \mu\mathrm{m} \tag{5}$$

$$\therefore A = 27.6\ \mathrm{MP\ m^{-3}\ \mu m^{-1}} \tag{6}$$

Because we consider all MPs between 1 and 100 µm diameter, this corresponds to a *total* number concentration of

$$N_{1-100} = \int_{0.5\ \mu\mathrm{m}}^{50\ \mu\mathrm{m}} 36.6\, r^{-1.52}\, \mathrm{d}r = 91.7\ \mathrm{MP\ m^{-3}} \tag{7}$$

for the power law size distribution, and

$$N_{1-100} = \int_{0.5\ \mu\mathrm{m}}^{50\ \mu\mathrm{m}} 27.6 \left(\frac{2r}{15}\right)^2 \frac{1}{r} e^{-2r/15}\, \mathrm{d}r = 27.3\ \mathrm{MP\ m^{-3}} \tag{8}$$

for the gamma size distribution. We use these values as the reference global-average surface MP number concentrations to which our radiative forcing results are scaled, and refer to both as "3.99 MP m^{-3} between 50 and 100 µm diameter" for simplicity.

As these concentrations are small and do not reliably produce a radiative forcing above the level of noise in the atmospheric model, we perform each simulation at an arbitrarily chosen global-average surface MP concentration ($[\mathrm{MP}]_{\mathrm{simulated}}$ in Equation (9) below). This concentration is chosen to produce a clear signal-to-noise ratio in the radiative forcing. Our reported radiative forcings are then rescaled to correspond to our reference global-average surface MP concentrations (N_{1-100} given above), assuming a linear relationship between the radiative forcing and the MP concentration.

This rescaling is described by Equation (5) in the main text, repeated here:

$$\mathrm{RF}_{\mathrm{scaled}} = \mathrm{RF}_{\mathrm{simulated}} \times \frac{[\mathrm{MP}]_{\mathrm{scaled}}}{[\mathrm{MP}]_{\mathrm{simulated}}} \tag{9}$$

where $[\mathrm{MP}]_{\mathrm{simulated}}$ is the arbitrarily chosen global-average surface MP concentration (listed in Table 2 of the main text); $[\mathrm{MP}]_{\mathrm{scaled}} = 27.3$ or 91.7 MP m^{-3} for the gamma or power law size distributions respectively; and $\mathrm{RF}_{\mathrm{simulated}}$ is the radiative forcing obtained in each simulation.

This is the same scaling procedure as used by Revell et al.[8], who used $[\mathrm{MP}]_{\mathrm{simulated}} = 100$ MP m^{-3} for all of their simulations. We found that, for our purposes, using the same $[\mathrm{MP}]_{\mathrm{simulated}}$ for all experiments did not produce a desirable signal-to-noise ratio due to differences in forcing efficiency between parameter settings. Consequently, we chose a unique $[\mathrm{MP}]_{\mathrm{simulated}}$ for each simulation.

We observed that the uncertainty produced by internal variability in the HadGEM3-GA7.1 model was largely independent of parameter settings, hence by targeting a particular radiative forcing magnitude we could achieve a uniform signal-to-noise ratio across experiments. For each experiment (Table 2 in the main text), we first estimated the IRF efficiency using the SOCRATES radiative transfer model. This then allowed the calculation of a value for $[\mathrm{MP}]_{\mathrm{simulated}}$ such that the expected radiative forcing was of a sufficient magnitude.

We chose a target radiative forcing magnitude of ± 200 mW m^{-2}. For the 'Previous estimate' simulation, this implied $[\mathrm{MP}]_{\mathrm{simulated}} = 1680$ MP m^{-3} (as given in Table 2 of the main text). The HadGEM3-GA7.1 simulation yielded a net effective radiative forcing of $\mathrm{RF}_{\mathrm{simulated}} = -157 \pm 45$ mW m^{-2} (as expected, close to our target radiative forcing). As the 'Previous estimate' simulation uses a gamma size distribution, $[\mathrm{MP}]_{\mathrm{scaled}} = 27.3$ MP m^{-3}, thus

$$\mathrm{RF}_{\mathrm{scaled}} = \left(-157 \pm 45 \text{ mW m}^{-2}\right) \times \frac{27.3 \text{ MP m}^{-3}}{1680 \text{ MP m}^{-3}} \tag{10}$$

$$= -2.55 \pm 0.73 \text{ mW m}^{-2} \tag{11}$$

as given in Table 1 of the main text.

Supplementary Fig. S4 shows the dependence of the MP net radiative forcing on the MP surface concentration. Radiative forcings were calculated for the 'Previous estimate' parameter scenario, i.e. colourless plastic, a gamma particle size distribution, a vertical distribution confined to < 2 km altitude, and a uniform surface concentration. The instantaneous radiative forcing (IRF) is extremely well fit by the linear regression. The effective radiative forcing (ERF) shows greater variation but the linear regression passes through the 5 to 95% confidence interval for each point, and the IRF linear regression falls within the 5 to 95% confidence interval of the ERF linear regression. This suggests that the assumption underlying Equation (9), i.e. proportionality between the MP radiative effect and the MP surface concentration, is valid for the forcing magnitudes we consider.

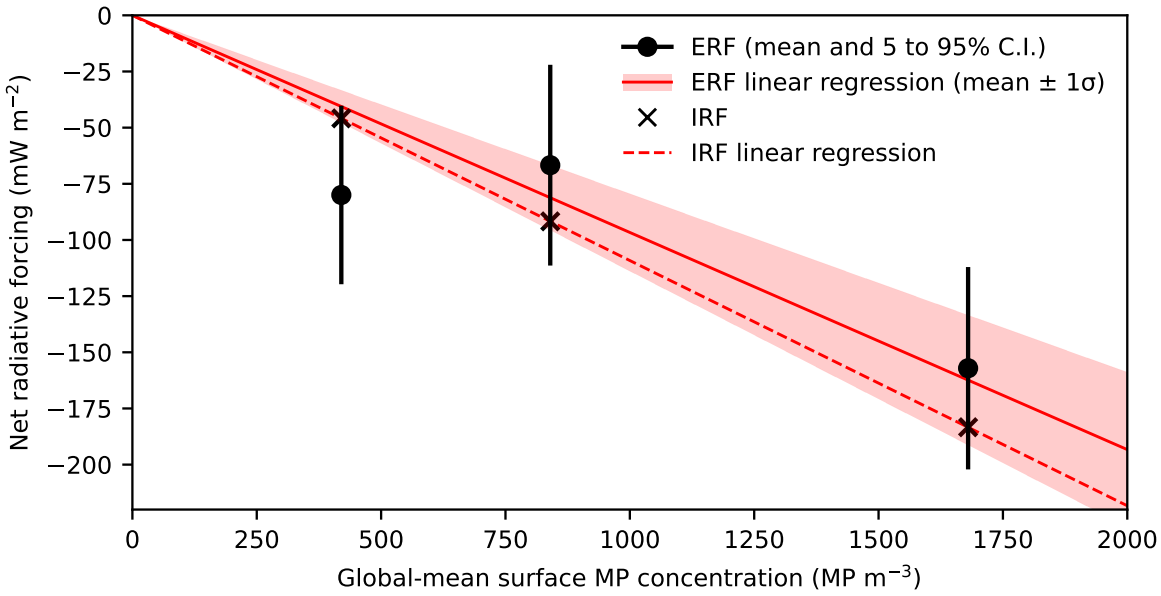

Figure S4: Dependence of MP net radiative forcing on surface MP concentration. All simulation parameters other than the surface MP concentration were set as in the 'Previous estimate' simulation (i.e. colourless plastic, a gamma size distribution, a vertical distribution confined to $<$ 2 km altitude, and a uniform spatial distribution). We constrain the linear regression to pass through the origin for physical consistency.

S5 Complex refractive index of coloured plastics

Supplementary Fig. S5 shows the complex refractive index of the different plastics considered in this work. They are: the colourless plastic considered by Revell et al.[8]; the colourless UV-absorbing plastic obtained from measurements of UV-absorption in plastic samples; the four coloured PET samples and the mixed colour, calculated as the average of the coloured plastics; and the colourless UV-absorbing plastic with 20% by weight black carbon included as homogeneous spheres. The calculation of these values is discussed in Section 4.1.3 of the main text.

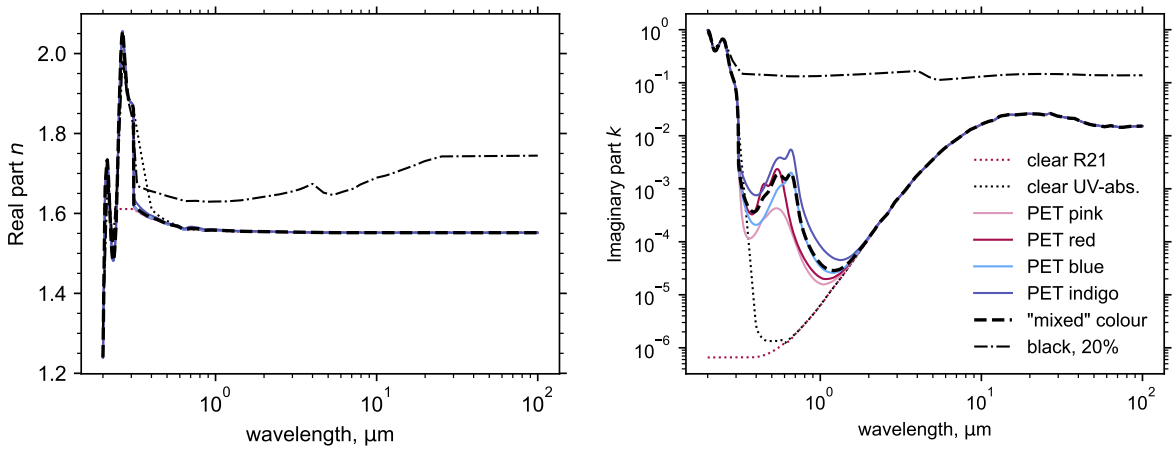

Figure S5: Complex refractive index $m = n + ik$ of different plastic colours in the UV-IR range of wavelengths.

References

[1] A. Chen, C. Zhao, H. Zhang, Y. Yang, and J. Li. Surface albedo regulates aerosol direct climate effect. *Nature Communications*, 15(1):7816, September 2024. ISSN 2041-1723. doi: 10.1038/s41467-024-52255-z.

[2] A. Chen, C. Zhao, L. Shen, and T. Fan. Influence of aerosol properties and surface albedo on radiative forcing efficiency of key aerosol types using global AERONET data. *Atmospheric Research*, 282:106519, February 2023. ISSN 0169-8095. doi: 10.1016/j.atmosres.2022.106519.

[3] J. Yoon, D. Y. Chang, J. Lelieveld, A. Pozzer, J. Kim, and S. S. Yum. Empirical evidence of a positive climate forcing of aerosols at elevated albedo. *Atmospheric Research*, 229:269–279, November 2019. ISSN 0169-8095. doi: 10.1016/j.atmosres.2019.07.001.

[4] H. Yang, Y. Xue, X. Sha, J. Yang, X. Wang, B. Suvdantsetseg, K. Kuroda, J. Pu, and L. Wang. Influence of regional environmental variables on the radiative forcing of atmospheric microplastics. *Eco-Environment & Health*, 4(1):100128, March 2025. ISSN 27729850. doi: 10.1016/j.eehl.2024.11.002.

[5] F. D. Leusch, H.-C. Lu, K. Perera, P. A. Neale, and S. Ziajahromi. Analysis of the literature shows a remarkably consistent relationship between size and abundance of microplastics across different environmental matrices. *Environmental Pollution*, 319:120984, February 2023. ISSN 02697491. doi: 10.1016/j.envpol.2022.120984.

[6] E. L. McGrath-Spangler and A. S. Denning. Global seasonal variations of midday planetary boundary layer depth from CALIPSO space-borne LIDAR. *Journal of Geophysical Research: Atmospheres*, 118(3):1226–1233, 2013. ISSN 2169-8996. doi: 10.1002/jgrd.50198.

[7] K. M. Chan and R. Wood. The seasonal cycle of planetary boundary layer depth determined using COSMIC radio occultation data. *Journal of Geophysical Research: Atmospheres*, 118 (22):12,422–12,434, 2013. ISSN 2169-8996. doi: 10.1002/2013JD020147.

[8] L. E. Revell, P. Kuma, E. C. Le Ru, W. R. C. Somerville, and S. Gaw. Direct radiative effects of airborne microplastics. *Nature*, 598(7881):462–467, October 2021. ISSN 0028-0836, 1476-4687. doi: 10.1038/s41586-021-03864-x.